The Astrophysical Journal, 843:76 (11pp), 2017 July 1 https://doi.org/10.3847/1538-4357/aa7461

The Fraction of Cool-core Clusters in X-Ray versus SZ Samples Using *Chandra* Observations

Felipe Andrade-Santos[1], Christine Jones[1], William R. Forman[1], Lorenzo Lovisari[1], Alexey Vikhlinin[1], Reinout J. van Weeren[1], Stephen S. Murray[1], Monique Arnaud[2], Gabriel W. Pratt[2], Jessica Démoclès[2], Ralph Kraft[1], Pasquale Mazzotta[1,3], Hans Böhringer[4], Gayoung Chon[4], Simona Giacintucci[5], Tracy E. Clarke[6], Stefano Borgani[7,8], Larry David[1], Marian Douspis[9], Etienne Pointecouteau[10,11], Håkon Dahle[12], Shea Brown[13], Nabila Aghanim[14], and Elena Rasia[8]
[1] Harvard-Smithsonian Center for Astrophysics, 60 Garden Street, Cambridge, MA 02138, USA; fsantos@cfa.harvard.edu
[2] Laboratoire AIM, CEA/IRFU, CNRS/INSU, Université Paris Diderot, CEA-Saclay, F-91191 Gif-Sur-Yvette, France
[3] Dipartimento di Fisica, Università di Roma Tor Vergata, via della Ricerca Scientifica 1, I-00133 Roma, Italy
[4] Max Planck Institute for Extraterrestrial Physics, Giessenbachstrasse, D-85748 Garching, Germany
[5] Naval Research Laboratory, 4555 Overlook Avenue SW, Code 7213, Washington, DC 20375, USA
[6] U.S. Naval Research Laboratory, Code 7213, 4555 Overlook Avenue SW., Washington, DC 20375, USA
[7] Dipartimento di Fisica dell' Università di Trieste, Sezione di Astronomia, via Tiepolo 11, I-34131 Trieste, Italy
[8] INAF, Osservatorio Astronomico di Trieste, via Tiepolo 11, I-34131, Trieste, Italy
[9] Institut d'Astrophysique Spatiale, CNRS (UMR8617) Université Paris-Sud 11, Bâtiment 121, Orsay, France
[10] CNRS; IRAP; 9 Av. colonel Roche, BP 44346, F-31028 Toulouse cedex 4, France
[11] Université de Toulouse; UPS-OMP; IRAP; Toulouse, France
[12] Institute of Theoretical Astrophysics, University of Oslo, P.O. Box 1029, Blindern, NO-0315 Oslo, Norway
[13] Department of Physics & Astronomy, The University of Iowa, Iowa City, IA 52245, USA
[14] Institut d'Astrophysique Spatiale, CNRS, Univ. Paris-Sud, Université Paris-Saclay, Bât. 121, F-91405 Orsay Cedex, France
Received 2017 March 24; revised 2017 May 3; accepted 2017 May 16; published 2017 July 5

Abstract

We derive and compare the fractions of cool-core clusters in the *Planck* Early Sunyaev–Zel'dovich sample of 164 clusters with $z \leqslant 0.35$ and in a flux-limited X-ray sample of 100 clusters with $z \leqslant 0.30$, using *Chandra* observations. We use four metrics to identify cool-core clusters: (1) the concentration parameter, which is the ratio of the integrated emissivity profile within 0.15 r_{500} to that within r_{500}; (2) the ratio of the integrated emissivity profile within 40 kpc to that within 400 kpc; (3) the cuspiness of the gas density profile, which is the negative of the logarithmic derivative of the gas density with respect to the radius, measured at 0.04 r_{500}; and (4) the central gas density, measured at 0.01 r_{500}. We find that the sample of X-ray-selected clusters, as characterized by each of these metrics, contains a significantly larger fraction of cool-core clusters compared to the sample of SZ-selected clusters (44% $\pm$ 7% versus 28% $\pm$ 4% using the concentration parameter in the 0.15–1.0 r_{500} range, 61% $\pm$ 8% versus 36% $\pm$ 5% using the concentration parameter in the 40–400 kpc range, 64% $\pm$ 8% versus 38% $\pm$ 5% using the cuspiness, and 53% $\pm$ 7% versus 39 $\pm$ 5% using the central gas density). Qualitatively, cool-core clusters are more X-ray luminous at fixed mass. Hence, our X-ray, flux-limited sample, compared to the approximately mass-limited SZ sample, is overrepresented with cool-core clusters. We describe a simple quantitative model that uses the excess luminosity of cool-core clusters compared to non-cool-core clusters at fixed mass to successfully predict the observed fraction of cool-core clusters in X-ray-selected samples.

Key words: galaxies: clusters: general – large-structure of universe

Supporting material: machine-readable tables

1. Introduction

Clusters of galaxies are the largest gravitationally bound structures in the universe. In the standard ΛCDM cosmology, massive halos dominated by dark matter assemble by the accretion of smaller groups and clusters (e.g., Forman & Jones 1982; Allen et al. 2011; Kravtsov & Borgani 2012). Under the influence of gravity, diffuse matter and smaller collapsed halos fall into larger halos, and occasionally halos of comparable mass merge with one another. X-ray observations of substructures in clusters of galaxies (see, for instance, Jones et al. 1979; Jones & Forman 1984; Mohr et al. 1995; Buote & Tsai 1996; Jones & Forman 1999; Jeltema et al. 2005; Böhringer et al. 2010; Laganá et al. 2010; Andrade-Santos et al. 2012, 2013) and measurements of the growth of structure (Vikhlinin et al. 2009b; Mantz et al. 2010; Allen et al. 2011; Benson et al. 2013; Planck Collaboration et al. 2014, 2016) demonstrate that clusters are still in the process of formation.

Early X-ray observations of galaxy clusters revealed that a significant fraction present a bright and dense core whose central cooling time is much shorter than the Hubble time. These observations led to the development of the cooling-flow model (Fabian & Nulsen 1977; Fabian et al. 1984; Fabian 1994, 2012). Analyzing deep *Chandra* observations of Hydra-A, David et al. (2001) showed that the spectral fits yielded significantly smaller mass deposition rates than expected. Using *XMM-Newton*, Peterson et al. (2003) presented high-resolution X-ray spectra of 14 putative cooling-flow clusters that exhibit a severe deficit of very cool emission relative to the predictions of the isobaric cooling-flow model. However, as predicted by the cooling-flow model, a temperature drop is observed in the center of many clusters, typically reaching one-third of the peak temperature (e.g., Peterson et al. 2003; Vikhlinin et al. 2005). Clusters presenting such a temperature drop in their cores are referred to as cool-core (CC) clusters (Molendi & Pizzolato 2001).

Using a very large, high-resolution cosmological *N*-body simulation (Millennium-XXL), Angulo et al. (2012) showed that cosmological conclusions based on galaxy cluster surveys depend critically on the selection biases, which include the wavelength used for the identification of clusters of galaxies. Planck Collaboration et al. (2011, 2013) presented the first observational evidence of different morphological properties in X-ray-selected versus SZ-selected samples: SZ-selected clusters have a less peaked density distribution and are less X-ray-luminous at a given mass than X-ray-selected clusters. Wen & Han (2013) presented a method to diagnose the substructure and dynamical states for 2092 optical galaxy clusters. They found that the fraction of relaxed clusters is 28% in the full sample, while the fraction increases to 46% for the subsample matched with *ROSAT* detections, indicating that the wavelength used for detecting clusters plays a significant role in the dynamical state of the population that is selected. McDonald et al. (2013) showed that CC clusters in his SZ sample represent 40% ± 10% of the cluster population at low redshift. Sommer & Basu (2014) constructed near-complete samples based on X-ray and SZ catalogs. They found that roughly 70% ± 10% of the clusters in the X-ray selection have no radio halos (indicating they are relaxed), whereas the fraction in the *Planck* selection is only 30 ± 10%, in agreement with findings from Wen & Han (2013) and McDonald et al. (2013).

More recently, Rossetti et al. (2016) compared the dynamical state of the 132 clusters with the highest signal-to-noise ratio from the *Planck* Sunyaev–Zel'dovich (SZ) catalog to that of three X-ray-selected samples (HIFLUGCS[15], MACS[16], and REXCESS[17]). They showed that the fractions of relaxed clusters in the the X-ray samples are significantly larger than those in the Planck sample, and interpreted this result to be an indication of a CC bias (Eckert et al. 2011) affecting X-ray selection.

Recently, Rossetti et al. (2017) compared the fraction of CC clusters in a Planck cosmology SZ sample (PSZ1, Planck Collaboration et al. 2014) to that in the MACS X-ray sample. Using the concentration parameter that measures the ratio of the integrated surface brightness in two fixed physical apertures, as defined by Santos et al. (2008), they showed that the CC fraction is significantly higher in the MACS X-ray-selected sample than in the Planck cosmology SZ sample (59% ± 5% in their X-ray sample versus 29% ± 4% in their SZ sample). This result agrees with that presented by Andrade-Santos et al. (2017), which is fully described in this paper. The X-ray sample presented in this paper spans a higher mass range compared to the mass range in the X-ray sample presented by Rossetti et al. (2017). Therefore, we also make use of three parameters that are computed at radii that scale with total mass. We note that the work presented by Rossetti et al. (2017) and the work presented here were developed in parallel (Jones et al. 2016; F. Andrade-Santos et al. 2017, in preparation).

In this paper we compare the nature of the cores for 164 *Planck* ESZ clusters at $z < 0.35$ to the 100 highest-flux X-ray clusters at Galactic latitudes $|b| > 20^\circ$ and $0.025 < z < 0.30$. The X-ray sample is extended to 100 clusters from the sample of 52 clusters presented by Voevodkin & Vikhlinin (2004) by lowering the flux limit to $f_X > 7.5 \times 10^{-12}$ erg s^{-1} cm^{-2} in the 0.5–2.0 keV band.

Throughout this paper, we assume a standard ΛCDM cosmology with $H_0 = 70$ km s^{-1} Mpc^{-1}, $\Omega_M = 0.3$, and $\Omega_\Lambda = 0.7$. All uncertainties are quoted at the 1σ level.

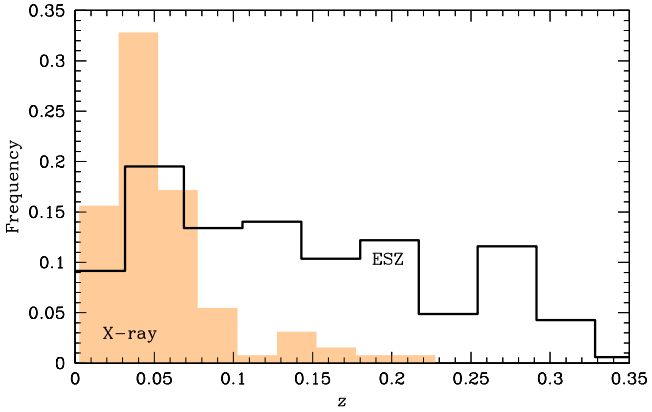

Figure 1. Distribution of cluster redshifts in the ESZ-selected and X-ray-selected samples. The ESZ sample extends to higher redshifts. The solid histogram shows the X-ray flux-limited sample, while the solid line corresponds to the ESZ cluster sample.

2. SZ and X-Ray-selected Clusters

The main goal of this work is to compare the fraction of CC clusters in X-ray-selected and SZ-selected samples. In this section, we describe the two samples.

2.1. SZ Sample

The first catalog of 189 SZ clusters detected by the *Planck* mission was released in early 2011 (Planck Collaboration et al. 2011). A *Chandra* XVP (X-ray Visionary Program—PI: Jones) and HRC Guaranteed Time Observations (PI: Murray) combined to form the *Chandra-Planck* Legacy Program for Massive Clusters of Galaxies.[18] For each of the 164 ESZ *Planck* clusters at $z \leqslant 0.35$, we obtained *Chandra* exposures sufficient to collect at least 10,000 source counts.

2.2. X-Ray Sample

Voevodkin & Vikhlinin (2004) compiled a sample of the X-ray-brightest clusters in the local universe by selecting the highest-flux clusters detected in the *ROSAT* All-Sky survey at $|b| > 20^\circ$ and $z > 0.025$—using the HIFLUGCS catalog (Reiprich & Böhringer 2002) as a reference. The sample used here is an extension of the Voevodkin & Vikhlinin (2004) sample, where the flux limit in the 0.5–2.0 keV band was lowered to $f_X > 7.5 \times 10^{-12}$ erg s^{-1} cm^{-2}. This sample contains 100 clusters and has an effective redshift depth of $z < 0.3$. All have *Chandra* observations. Of the 100 X-ray-selected clusters, 49 are also in the ESZ sample, and 47 are in the HIFLUGCS catalog.

2.3. Comparisons between the X-Ray-selected and ESZ-Selected Clusters

Figure 1 presents the redshift distribution in both samples. The *Planck*-detected clusters are clearly more broadly distributed in redshift than the X-ray clusters. This is due to the

[15] HIFLUGCS—The HIghest X-ray FLUx Galaxy Cluster Sample (Reiprich & Böhringer 2002).
[16] MACS—The MAssive Cluster Survey (Ebeling et al. 2001).
[17] REXCESS—The REpresentative XMM-Newton ClustEr Structure Survey (Böhringer et al. 2007).
[18] hea-www.cfa.harvard.edu/CHANDRA_PLANCK_CLUSTERS/

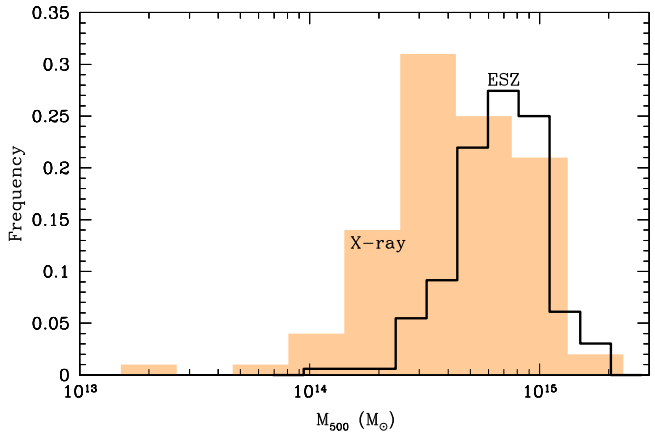

Figure 2. Distribution of cluster masses within r_{500} for the ESZ-selected and X-ray-selected samples (see Sections 2.1 and 2.2). The X-ray sample extends to lower masses than the ESZ sample. The solid histogram shows the X-ray flux-limited sample, while the solid line corresponds to the ESZ cluster sample.

nature of the selection. For resolved clusters the Sunyaev–Zel'dovich signal is independent of the redshift of the cluster because it is the CMB that is distorted (the CMB photons originated at the epoch of recombination—from a constant redshift of $z \sim 1000$), while the X-ray selected clusters constitute a flux-limited sample, which strongly favors the X-ray-brighter, lower-redshift clusters. Figure 2 presents the mass distribution of both samples. The X-ray sample spans a much larger mass range, extending to lower masses than the *Planck* ESZ sample. The difference between the lowest observed mass in the X-ray and ESZ samples is caused by different detection thresholds. Note that the highest observed mass is the same for both samples (see Figure 2).

2.4. Subclusters

A small fraction (∼10%–20%) of the clusters in both the X-ray and SZ samples present X-ray-bright subclusters. In our analyses we exclude the secondary subclusters. Only the principal cluster component is used in the comparisons between the X-ray and SZ samples. However, we present the metrics for all cluster components in Tables 4 and 5.

3. Data Reduction

Our *Chandra* data reduction followed the process described in Vikhlinin et al. (2005). We applied the calibration files `CALDB 4.7.2`. The data reduction included corrections for the time dependence of the charge transfer inefficiency and gain, and also a check for periods of high background, which were then omitted. Standard blank sky background files and readout artifacts were subtracted. We also detected compact X-ray sources in the 0.7–2.0 keV and 2.0–7.0 keV bands using CIAO wavdetect and then masked these sources before performing the spectral and spatial analyses of the cluster emission. For each cluster, we used all available *Chandra* observations within 2 Mpc of the cluster center with all CCDs (ACIS-I and ACIS-S).

4. Emission Measure Profiles

We refer to Vikhlinin et al. (2006) for a detailed description of the procedures we used to compute the emission measure profile for each cluster. We outline here only the main aspects of the method.

We measured the surface brightness profiles in the 0.7–2.0 keV energy band, which maximizes the signal-to-noise ratio in *Chandra* observations for typical cluster gas temperatures. We used the X-ray halo peak as the cluster center. The readout artifacts and blank-field background (see Section 2.3.3 of Vikhlinin et al. 2006) were subtracted from the X-ray images, and the results were then exposure-corrected, using exposure maps computed assuming an absorbed optically thin thermal plasma with $kT = 5.0$ keV, abundance $= 0.3$ solar, with the Galactic column density and including corrections for bad pixels and CCD gaps, which do not take into account spatial variations of the effective area. We subtracted any small uniform component corresponding to soft X-ray foreground adjustments, if required (determined by fitting a thermal model in a region of the detector field distant from the cluster center, taking into account the expected thermal contribution from the cluster).

Following these steps, we extracted the surface brightness in narrow concentric annuli ($r_{\rm out}/r_{\rm in} = 1.05$) centered on the X-ray halo peak and computed the *Chandra* area-averaged effective area for each annulus (see Vikhlinin et al. (2005), for details on calculating the effective area). To compute the emission measure and temperature profiles, we assumed spherical symmetry. The spherical assumption is expected to introduce only small deviations in the emission measure profile (Piffaretti et al. 2003). Using the modeled deprojected temperature (see Section 7), effective area, and metallicity as a function of radius, we converted the *Chandra* count rate in the 0.7–2.0 keV band into the emission integral, $\mathrm{EI} = \int n_{\rm e} n_{\rm p} dV$, within each cylindrical shell. Tables 4 and 5 list the maximum cluster radius where the emission integral is computed ($r_{\rm max}$) for each cluster. Seven clusters in the ESZ sample have $r_{\rm max} < r_{500}$, and in the X-ray sample, nine clusters have this condition (four of them are also in the ESZ sample). These numbers represent only 4% and 9% of the clusters in the ESZ and X-ray samples, respectively.

We fit the emission measure profile assuming the gas density profile follows that given by Vikhlinin et al. (2006):

$$n_{\rm e} n_{\rm p} = n_0^2 \frac{(r/r_{\rm c})^{-\alpha}}{(1 + r^2/r_{\rm c}^2)^{3\beta-\alpha/2}} \frac{1}{(1 + r^\gamma/r_{\rm s}^\gamma)^{\epsilon/\gamma}} + \frac{n_{02}^2}{(1 + r^2/r_{\rm c2}^2)^{3\beta_2}}, \quad (1)$$

where the parameters n_0 and n_{02} determine the normalizations of both additive components. α, β, β_2, and ϵ are indexes controlling the slope of the curve at characteristic radii given by the parameters $r_{\rm c}$, $r_{\rm c2}$, and $r_{\rm s}$. γ controls the width of the transition region given by $r_{\rm s}$. Although the relation given by Equation (1) is based on a classic β-model (Cavaliere & Fusco-Femiano 1976), it is modified to account for a central power-law type cusp and a steeper emission measure slope at large radii. In addition, a second β-model is included, to better characterize the cluster core. For further details on this equation, we refer the reader to Vikhlinin et al. (2006). In the fit to the emissivity profile, all parameters are free to vary. For a typical metallicity of 0.3 $Z_\odot$, the reference values from Anders & Grevesse (1989) yield $n_{\rm e}/n_{\rm p} = 1.1995$. Examples of

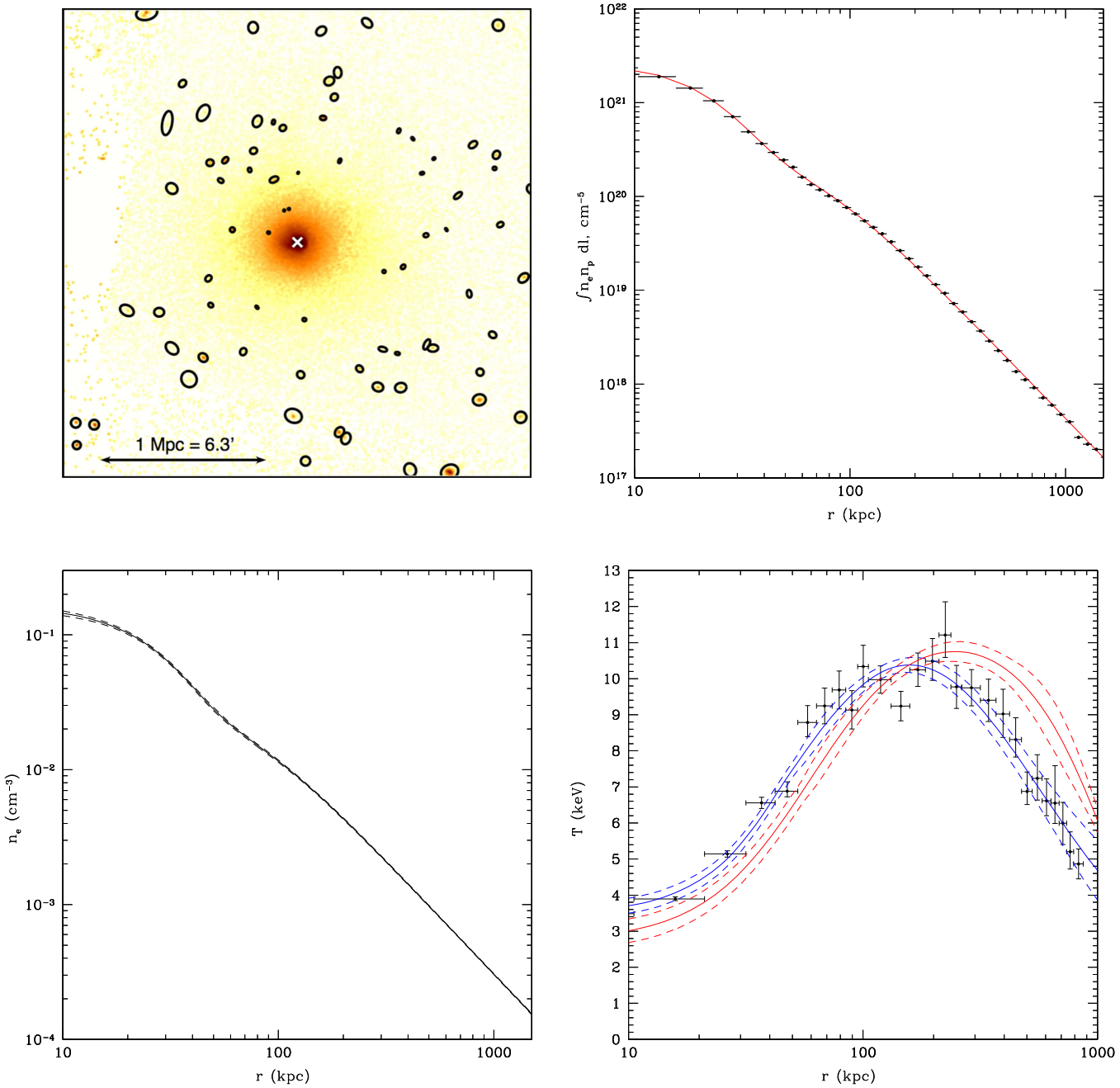

Figure 3. Example of the X-ray image and the projected emissivity, gas density, and temperature profiles for a CC cluster (A2204). The top left panel shows the 0.5–2.0 keV, background-subtracted, exposure-map-corrected ACIS-I image. The total filtered *Chandra* exposure is 117 ks. The black ellipses correspond to the masked X-ray point sources and the cross corresponds to the cluster center. The top right panel shows the projected emissivity profile. The solid line shows the emission measure integral of the best fit to the emissivity profile given by Equation (1). The bottom left panel shows the gas density profile. The solid line shows the density profile obtained from the emissivity profile given by Equation (1). The bottom right panel shows the gas temperature profile. The red and blue lines show the deprojected and projected temperature profiles, respectively (Equations (7) and 8). The dashed lines in the gas and temperature profiles show the 68% confidence range. This is an example of a cluster with deep *Chandra* exposure, which allow us to extract the temperature profile in many radial bins.

projected emissivity and gas density profiles are presented in Figures 3 and 4.

5. Total Cluster Mass Estimates

Using the gas mass and temperature, we estimated the total cluster mass from the Y_X–M scaling relation of Vikhlinin et al. (2009a),

$$M_{500,Y_X} = E^{-2/5}(z) A_{YM} \left(\frac{Y_X}{3 \times 10^{14} M_\odot \mathrm{keV}} \right)^{B_{YM}}, \quad (2)$$

where $Y_X = M_{gas,500} \times kT_X$, $M_{gas,500}$ is computed using the best-fit parameters of Equation (1), and T_X is the measured temperature in the $(0.15–1) \times r_{500}$ range. $A_{YM} = 5.77 \times 10^{14} h^{1/2} M_\odot$ and $B_{YM} = 0.57$ (Maughan et al. 2012). Here, $M_{Y_X,500}$ is the total mass within r_{500}, and $E(z) = [\Omega_M(1+z)^3 + (1-\Omega_M-\Omega_\Lambda)(1+z)^2 + \Omega_\Lambda]^{1/2}$ is the function describing the evolution of the Hubble parameter.

Using Equation (2), r_{500} is computed by solving

$$M_{500,Y_X} \equiv 500 \rho_c (4\pi/3) r_{500}^3, \quad (3)$$

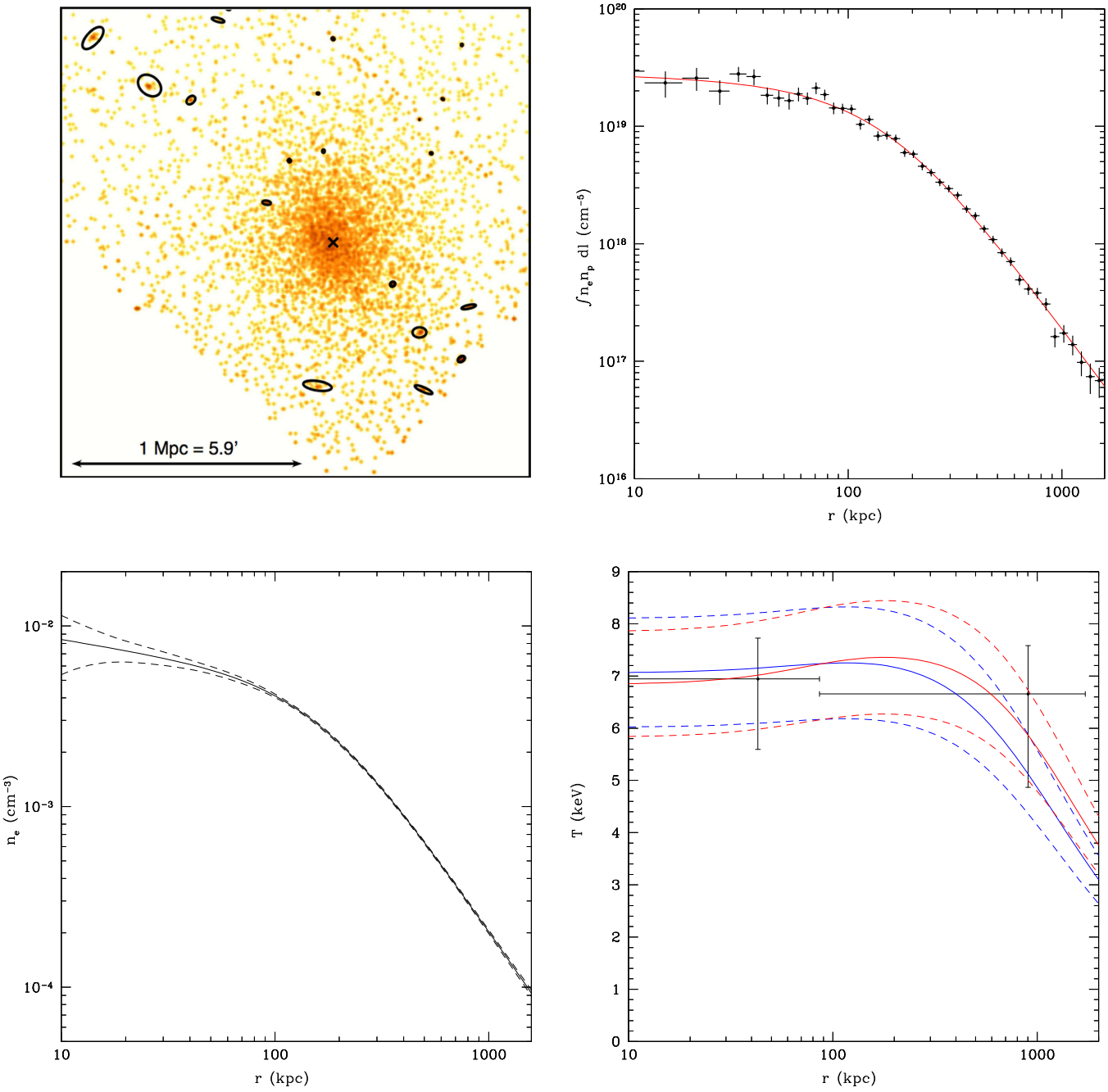

Figure 4. Similar panels as in Figure 3, for the non-CC cluster PLCKESZ G000.44-41.83. This is an example of a cluster with moderate data quality, which illustrates the necessity of metrics to determine the nature of the cluster core in the absence of a detailed temperature profile, like that shown in Figure 3. The total filtered *Chandra* exposure is 14 ks.

where ρ_c is the critical density of the universe at the cluster redshift. In practice, Equation (2) is evaluated at a given radius, whose result is compared to the evaluation of Equation (3) at the same radius. This process is repeated in an iterative procedure, until the fractional mass difference is less than 1%.

6. Cool-core Metrics

It is not possible to measure the temperature profile to determine the presence of a cool core for all clusters in our SZ and X-ray samples because of the X-ray data quality. Figures 3 and 4 illustrate the difference in data quality in the sample. Instead, we apply a more robust approach of using four metrics, described below, to characterize the presence of cool cores.

6.1. Concentration Parameter in the 40–400 kpc Range

The presence of cooler gas in the cores of clusters usually implies a larger gas density in the core, compared to the gas density outside the core, to maintain the pressure balance. This

increased gas density produces an X-ray-bright core, since the X-ray emissivity is roughly proportional to the square of the gas density. Evaluating the X-ray brightness in the cluster core compared to the brightness within a given larger radius is a powerful method to determine if the cluster contains a cool core. This metric is referred to as the concentration parameter and was originally introduced by Santos et al. (2008):

$$C_{\rm SB4} = \frac{\Sigma(<40\ {\rm kpc})}{\Sigma(<400\ {\rm kpc})}, \quad (4)$$

where $\Sigma(<r)$ is the integrated projected emissivity within a circle of radius r.

6.2. Concentration Parameter in the 0.15–1.0 r_{500} Range

Here we also use a modification of the original definition (Santos et al. 2008), which is scaled by the characteristic radius r_{500} as (Maughan et al. 2012):

$$C_{\rm SB} = \frac{\Sigma(<0.15r_{500})}{\Sigma(<r_{500})}. \quad (5)$$

6.3. Cuspiness of the Gas Density Profile

A third related metric is the cuspiness of the gas density profile computed at a fixed scaled radius of $0.04r_{500}$ (Vikhlinin et al. 2007):

$$\delta = -\frac{d\ \log n(r)}{d\ \log r}\ \Big|\ r = 0.04r_{500}, \quad (6)$$

where $n(r)$ is the gas density at a distance r from the cluster center.

6.4. Central Gas Density

A fourth useful quantity that indicates if a cluster presents a cool core is the central gas density (Hudson et al. 2010). Here we calculate the central density at 0.01 r_{500} from the core (which will be called $n_{\rm core}$), since the equation used to fit the density profile may diverge at $r = 0$ (if $\alpha > 0$ in Equation (1)).

7. Temperature Profiles

In this paper, we present the temperature profiles for only two clusters, although we have temperature profiles for all clusters in our samples, which vary in the number of fitted parameters according to the quality of the data. We provide the fitted parameters for all clusters in Andrade-Santos et al. (2017). The two temperature profiles presented in this paper are examples of CC and non-CC (NCC) clusters as well as clusters with very different data quality (see Figures 3 and 4). In this section, we present the analytic equations used to obtain the profiles, referring the reader to papers where the full descriptions of the calculations are presented (see Vikhlinin et al. 2006; Andrade-Santos et al. 2015, 2016).

Vikhlinin et al. (2006) give a 3D temperature profile that describes the general features of the temperature profile of clusters:

$$T_{\rm 3D}(r) = T_0 \times \frac{x + T_{\rm min}/T_0}{x+1} \times \frac{(r/r_{\rm t})^{-a}}{(1+(r/r_{\rm t})^b)^{c/b}}, \quad (7)$$

where $x = (r/r_{\rm cool})^{a_{\rm cool}}$. $r_{\rm t}$ and $r_{\rm cool}$ are the transition and CC radii, respectively. $T_{\rm min}$ is the central temperature, and a, b, c, and $a_{\rm cool}$ are indexes that determine the slopes of the temperature profile in different radial ranges.

We derive the deprojected 3D temperature by projecting a model to compare to the projected measured temperature. The 3D temperature model, $T_{\rm 3D}$, is weighted by the density squared according to the spectroscopic-like temperature (Mazzotta et al. 2004 presented a formula to project the temperature that matches the spectroscopically measured temperature within a few percent):

$$T_{\rm 2D} = T_{\rm spec} \equiv \frac{\int n_{\rm e}^2 T_{\rm 3D}^{1/4} dz}{\int n_{\rm e}^2 T_{\rm 3D}^{-3/4} dz}, \quad (8)$$

to give values of T_{2D} for comparison with the measured values. $n_{\rm e}$ is the electron density, given by Equation (1), and $T_{\rm 3D}$ is the deprojected 3D temperature, given by Equation (7).

8. Results

With the cluster gas density and emission measure profiles, we are able to compute the cuspiness of the gas density profile, concentration, and central gas density for the X-ray and *Planck* ESZ cluster samples. The uncertainties on the metrics for each cluster were computed using 100 Monte Carlo realizations of the density profile, also including a Gaussian distribution for r_{500} ($r_{500} \pm \sigma_{r_{500}}$). The top left panel of Figure 5 presents the distribution of concentration parameters in the 0.15–1.0 r_{500} range for both cluster samples. We used a Kolmogorov–Smirnov (K–S) test for the SZ and X-ray samples to evaluate the probability that the two samples were drawn from the same distribution. We obtained p-values that are smaller than 3.1×10^{-2} for all metrics, which suggests that the fraction of cool cores in the sample of X-ray-selected clusters is different from that in the SZ sample. Defining a CC cluster as one that presents a concentration parameter in the 0.15–1.0 r_{500} range, $C_{\rm SB} > 0.4$, the fraction of cool cores in the X-ray sample is $44\% \pm 7\%$, whereas in the SZ sample, the fraction is $28\% \pm 4\%$. The uncertainties on the fraction of CC clusters were computed using a Bootstrap re-sampling method, including Poisson statistics on the number of clusters satisfying the CC criterion: a metric value greater than the break value used to segregate clusters into CC and NCC. With a break value of 0.075 (Santos et al. 2008) for the concentration parameter in the 40–400 kpc range (Figure 5, top right panel), we have a CC fraction of $61 \pm 8\%$ in the X-ray sample and $36 \pm 5\%$ in the SZ sample. The high fraction of CC clusters in the X-ray selected sample compared to that in the SZ sample agrees quite well with the recent results presented by Rossetti et al. (2017) ($59\% \pm 5\%$ in their X-ray sample versus $29\% \pm 4\%$ in their SZ sample). With a break value of 0.5 (Vikhlinin et al. 2007) for the cuspiness of the gas density profile (Figure 5, bottom left panel), we have a CC fraction of $64\% \pm 8\%$ in the X-ray sample and $38\% \pm 5\%$ in the SZ sample. Maughan et al. (2012) used a value of 0.8, more appropriate for moderate to strong CC clusters. They also used a break value of 0.5 for the concentration parameter in the 0.15–1.0 r_{500} range, which we chose to be 0.4 to also include weak CC clusters. Finally, using a break value of $1.5 \times 10^{-2}\ {\rm cm}^{-3}$ (Hudson et al. 2010) for the central gas density to distinguish CC and NCC clusters (Figure 5, bottom right panel), we find that $53\% \pm 7\%$ of the clusters in the X-ray sample have cool cores, whereas the SZ sample shows a fraction of $39\% \pm 5\%$. The fractions of CC clusters and K–S

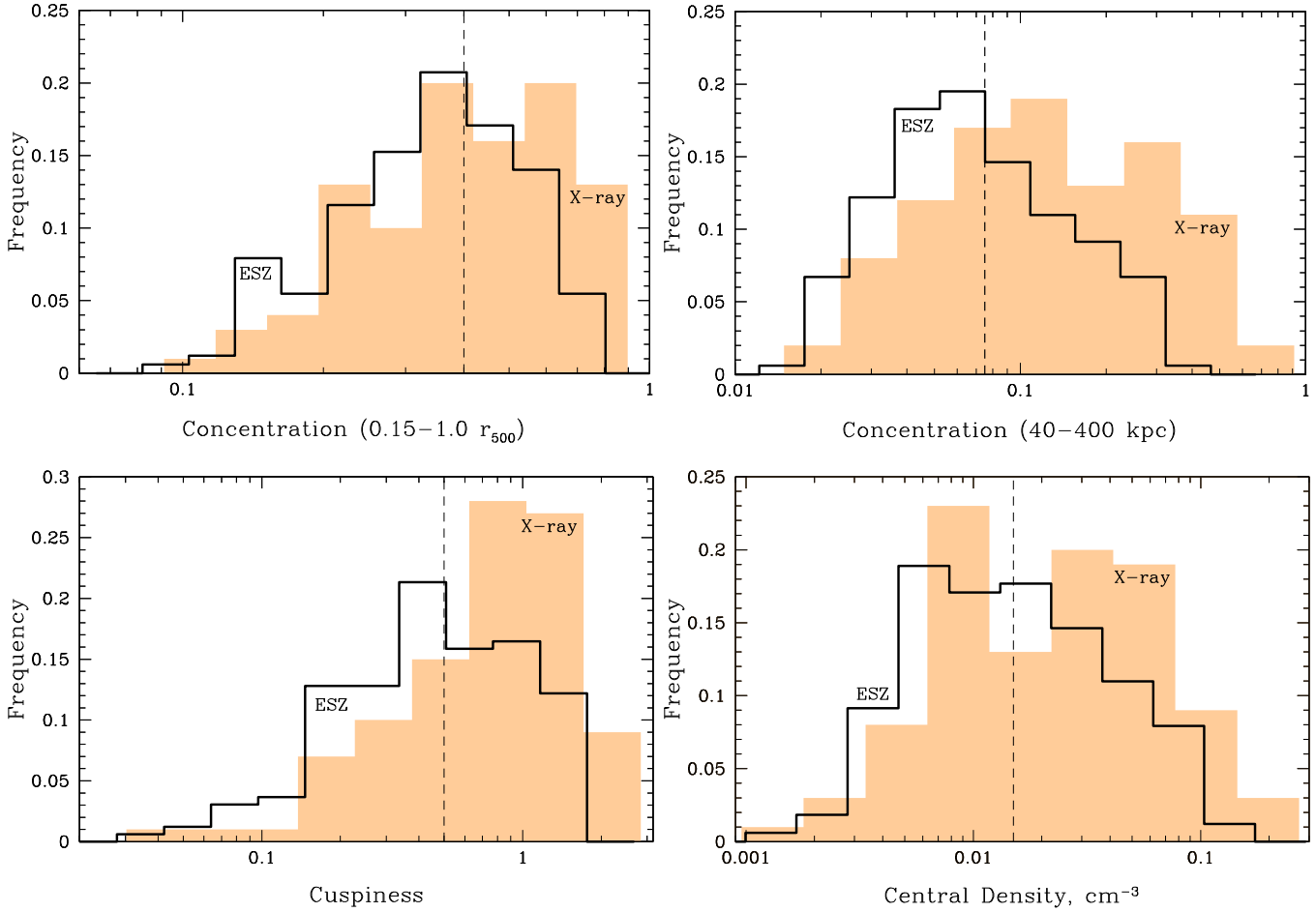

Figure 5. Top left: distribution of the concentration parameter in the 0.15–1.0 r_{500} range (C_{SB}—see Equation (5)) for the 164 *Planck* ESZ-selected (solid line) and the 100 X-ray-selected clusters (orange shaded). Top right: distribution of the concentration parameter in the 40–400 kpc range (C_{SB4}—see Equation (4)) for both samples. Bottom left: distribution of the cuspiness (δ—see Equation (6)) for both samples. Bottom right: distribution of the central density (n_{core}) for both samples. The dashed vertical line in each panel corresponds to the break value used to segregate clusters into CC and NCC subsamples (0.4 for the concentration parameter in the 0.15–1.0 r_{500} range, 0.075 for the concentration parameter in the 40–400 kpc range, 0.5 for the cuspiness, and 1.5×10^{-2} cm^{-3} for the central gas density).

Table 1
Cool-core Metrics Systematic Uncertainty is Computed by Varying the Break Value by ±10%

Metric	K–S p-value	Break Value	CC fraction X-ray (%)	CC fraction ESZ (%)
C_{SB}: Concentration (0.15–1.0 r_{500})	3.1×10^{-2}	0.4	44 ± 7 (sys $^{+6}_{-6}$)	28 ± 4 (sys $^{+10}_{-6}$)
C_{SB4}: Concentration (40–400 kpc)	2.9×10^{-4}	0.075	61 ± 8 (sys $^{+3}_{-5}$)	36 ± 5 (sys $^{+4}_{-4}$)
δ: Cuspiness	1.1×10^{-4}	0.5	64 ± 8 (sys $^{+3}_{-4}$)	38 ± 5 (sys $^{+4}_{-4}$)
n_{core}: Central Density	1.9×10^{-2}	1.5×10^{-2} cm^{-3}	53 ± 7 (sys $^{+3}_{-2}$)	39 ± 5 (sys $^{+3}_{-3}$)

test results are listed in Table 1. We also include in Table 1 a systematic uncertainty on the fraction of CC clusters by varying the break value by ±10%. The magnitude of this systematic uncertainty is comparable to the statistical uncertainty.

Using all four comparisons of the X-ray and SZ cluster samples, we find that CC clusters are significantly more common in X-ray-selected cluster samples than in SZ-selected samples.

Figure 6 shows the correlations between all metrics. Visually, we observe a strong correlation between all metrics, which we verified numerically using a Spearman test. This provides a correlation coefficient ranging between 0 (no correlation) and (−)+1, in the case of perfect (anti)correlation. Results for our metrics are listed in Table 2.

Using a set of cosmological hydrodynamic simulations of galaxy clusters, Rasia et al. (2015) found that 38% (11/29) of their simulated clusters at $z = 0$ are classified as CC using the central entropy (Cavagnolo et al. 2009) and pseudo-entropy ratio (Leccardi et al. 2010) as metrics. This result agrees very well with our observed fraction of CC clusters in the SZ sample (28%–39% according to the metric used, suggesting that the fraction of CC clusters in SZ samples is representative of the fraction of CC clusters in the universe). Lin et al. (2015) showed that constraints on the fraction of CC clusters in SZ-selected data sets are only subject to a systematic bias of the order of one percent, a significant reduction compared to X-ray-selected samples, supporting that SZ-selected samples of galaxy clusters are robust cosmological probes.

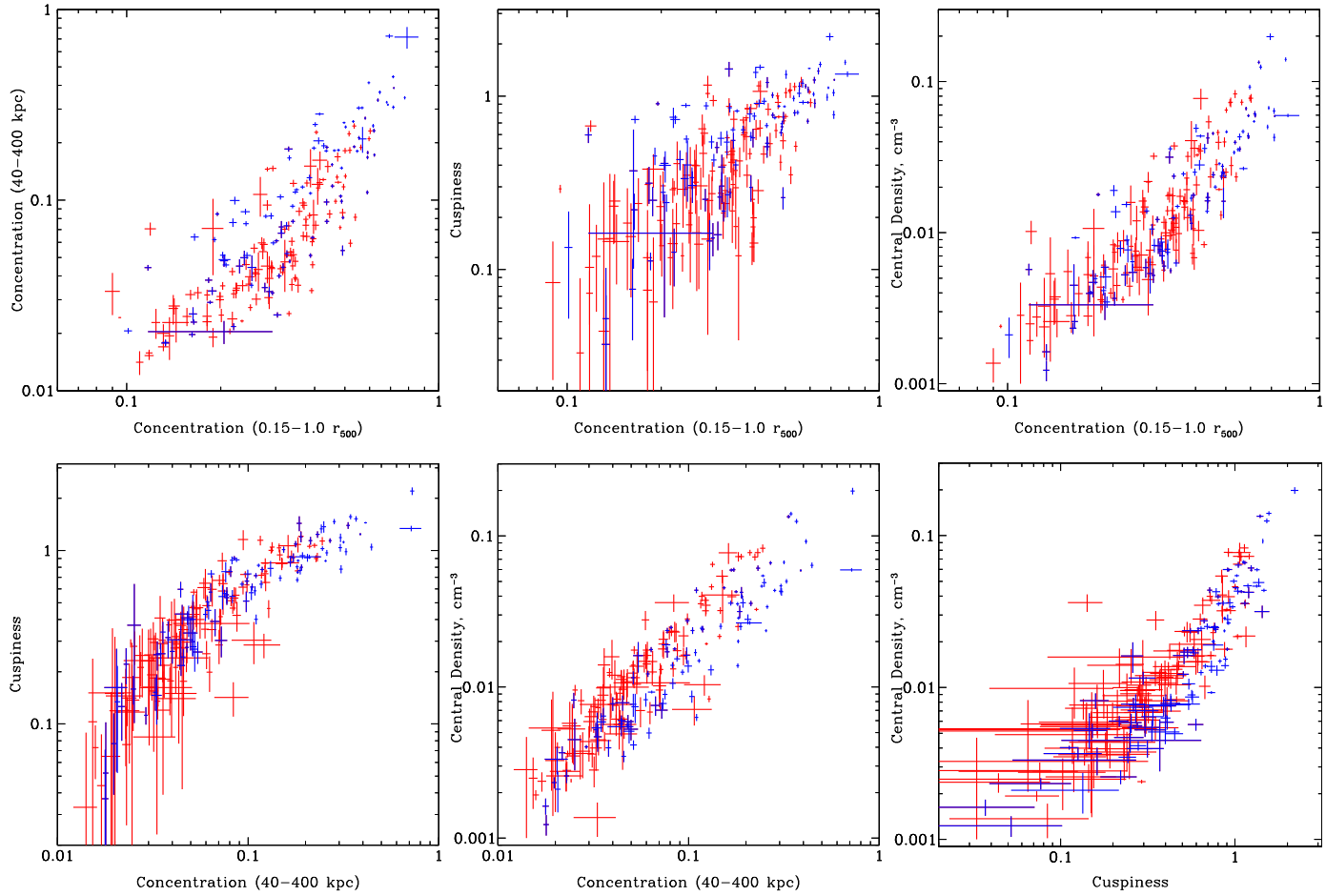

Figure 6. Top left: concentration parameter in the 40–400 kpc range (C_{SB4}) vs. concentration parameter in the 0.15–1.0 r_{500} range (C_{SB}). Top center: cuspiness (δ) vs. concentration parameter in the 0.15–1.0 r_{500} range (C_{SB}). Top right: central density (n_{core}) vs. concentration parameter in the 0.15–1.0 r_{500} range (C_{SB}) . Bottom left: cuspiness (δ) vs. concentration parameter in the 40–400 kpc range (C_{SB4}). Bottom center: central density (n_{core}) vs. concentration parameter in the 40–400 kpc range (C_{SB4}). Bottom right: central density (n_{core}) vs. cuspiness (δ). The ESZ sample is in red and the X-ray sample is in blue. This figure shows the strong correlation between different metrics, whose correlations are quantified in Table 2.

Table 2
Spearman Rank Test

Relation	Correlation (X-Ray)	Correlation (ESZ)
C_{SB} versus C_{SB4}	0.87	0.84
C_{SB} versus δ	0.75	0.69
C_{SB} versus n_{core}	0.90	0.87
C_{SB4} versus δ	0.93	0.90
C_{SB4} versus n_{core}	0.93	0.91
δ versus n_{core}	0.92	0.88

8.1. Numerical Simulations

In this section, we apply the four metrics used in this paper to the set of numerical simulations of galaxy clusters from Rasia et al. (2015). We obtain the following results: (a) using the concentration parameter in the 0.15–1.0 r_{500} range, we obtain a fraction of CC clusters of 33% ± 11%, (b) using the concentration parameter in the 40–400 kpc range, the fraction of CC clusters is 26% ± 10%, (c) using the cuspiness of the gas density, the fraction of CC clusters is 38% ± 11%, and (d) using the central gas density, the fraction of CC clusters is 48% ± 13%. These numbers are in good agreement with the fraction of CC clusters in our ESZ sample.

9. Selection Effects: Malmquist Bias in X-Rays

The X-ray cluster sample used in this paper is derived from the *ROSAT* X-ray catalogs, which formally used the total X-ray flux as the only selection criterion. Thus, it can be affected by the Malmquist bias, leading to overrepresentation of the CC clusters. CC clusters tend to be more X-ray-luminous for the same mass and thus they become overrepresented in a purely X-ray, flux-limited survey. To estimate the fractional increase in the X-ray luminosity of the CC subsample, we compare the ratio of the observed luminosity to the expected luminosity for the measured mass (using the L_X–M relation given by Equation (22) from Vikhlinin et al. 2009a) for CC and NCC clusters for all four metrics used to identify CC clusters. We find that CC clusters are on average ∼1.6–1.8 times more X-ray-luminous for the same mass (Table 3) than are NCC clusters. These results are consistent with early studies based on *Einstein* imaging data (central excesses over the β-model, Jones & Forman 1999), and normalizations of the L_X—T relations for the CC and NCC populations (Allen & Fabian 1998).

The impact of this difference in the total X-ray luminosity on the fractions of CC and NCC clusters is substantial. In a low-z flux-limited survey, the search volume is $\propto L^{3/2}$,so a subpopulation that is intrinsically more luminous by a factor of

Table 3
Overpopulation of CC Clusters

Metric	$\langle L_{CC}\rangle/\langle L_{NCC}\rangle$	Expected Overpopulation	Observed Overpopulation
C_{SB}	1.80 ± 0.16	2.7 ± 1.0	1.6 ± 0.3
C_{SB4}	1.63 ± 0.15	2.3 ± 0.7	1.7 ± 0.3
δ	1.57 ± 0.15	2.1 ± 0.7	1.7 ± 0.3
n_{core}	1.69 ± 0.15	2.4 ± 0.8	1.4 ± 0.3

$\sim$1.7 becomes overrepresented by a factor of 2.2 above a fixed mass threshold.

A similar bias is still present if we consider clusters in a narrow redshift range, where there is no difference in the search volume. In this case, a flux limit is equivalent to an X-ray luminosity threshold. CC clusters are less massive than NCC clusters for a fixed L_X and hence are more numerous than NCC clusters.

We can quantify the selection effects of CC clusters in X-ray surveys. For simplicity, let us approximate the cluster mass function locally as a power law given by:

$$N(>M) \propto M^{-\gamma}, \tag{9}$$

and assume a power law M–L_X relation as:

$$L_X \propto M^{\beta}. \tag{10}$$

Let l be the ratio of average luminosities (0.5–2.0 keV band, in the 0–r_{500} range) at a fixed mass for the CC and NCC populations:

$$l \equiv \langle L_{CC}\rangle / \langle L_{NCC}\rangle, \tag{11}$$

then we would expect the ratio of the number of CC to NCC clusters to be:

$$\Delta \equiv l^{\gamma/\beta}. \tag{12}$$

We computed the ratio of average luminosities at a fixed mass for the CC and NCC populations, l, to be in the range 1.6–1.8 (Table 3). From Vikhlinin et al. (2009a), $\beta = 1.61 \pm 0.14$. To compute the slope of the halo mass function, we averaged the slope of the mass function at the location of each cluster mass in our X-ray sample, using the mass function provided by Warren et al. (2006). We obtained $\gamma = 2.54 \pm 0.79$. With these numbers in hand, we estimate that the CC clusters are overrepresented in our X-ray sample by a factor of $\Delta = 2.1$–2.7 (depending on the metric) because of the Malmquist bias.

10. Conclusions

Using *Chandra* observations, we derived and compared the fraction of CC clusters in the *Planck* Early Sunyaev–Zel'dovich (ESZ) sample of 164 detected clusters with $z \leqslant 0.35$ and in a flux-limited X-ray sample of 100 clusters with $z \leqslant 0.30$. We use four metrics to identify the presence of a cool core: (1) the concentration parameter, which is the ratio of the integrated surface brightness within 0.15 r_{500} to that within r_{500}; (2) within 40 kpc to that within 400 kpc; (3) the cuspiness of the gas density profile, which is the negative of the logarithmic derivative of the gas density with respect to the radius measured at 0.04 r_{500}; and (4) the central gas density, measured at 0.01 r_{500}. We list our findings.

1. In all four metrics that we used, the sample of X-ray-selected clusters contains a significantly larger fraction of CC clusters compared to the sample of SZ-selected clusters (44% $\pm$ 7% versus 28% $\pm$ 4% using the concentration parameter in the 0.15–1.0 r_{500} range as a metric for cool cores, 61% $\pm$ 8% versus 36% $\pm$ 5% using the concentration parameter in the 40–400 kpc range, 64% $\pm$ 8% versus 38% $\pm$ 5% using the cuspiness, and 53% $\pm$ 7% versus 39% $\pm$ 5% using the central density). Our results for the concentration parameter in the 40–400 kpc range agree well with the recent results by Rossetti et al. (2017).
2. Qualitatively, CC clusters are more X-ray-luminous at fixed mass. Hence, our X-ray flux-limited sample, compared to the approximately mass-limited SZ sample, is overrepresented with CC clusters. We describe a simple quantitative model that successfully predicts the observed difference based on the selection bias. Our model predicts an overpopulation of CC clusters in our X-ray-selected sample compared to SZ samples of 2.1–2.7, depending on the metric used to identify CC clusters, with a typical uncertainty of $\sim$0.8, which is consistent within the uncertainties with the observed values in the range 1.4–1.7, with a typical uncertainty of $\sim$0.3.
3. The results of the four metrics we used to measure the overpopulation of CC clusters in X-ray samples, compared to the results for SZ samples, are all consistent within their uncertainties.
4. While differences in X-ray and SZ cluster selection are significant, they can be quantitatively explained by the effect of cool cores on X-ray luminosities.

CC clusters are more X-ray luminous than NCC clusters for a fixed cluster mass. Thus, an X-ray flux-limited sample will select a larger fraction of CC clusters compared to an SZ-selected cluster sample. The determination of cosmological parameters from an X-ray flux-limited sample in the local universe can be summarized by determining confidence levels in the highly degenerate Ω_M–σ_8 plane. If cluster masses are determined using a proxy other than the X-ray luminosity (e.g., gas mass, M–Y_X scaling relation, T_X, weak-lensing, hydrostatic mass) there will be no Malmquist bias on the determination of cosmological parameters, simply because when the mass function is constructed, the CC clusters that were wrongly included in the selection will now be excluded from the mass function because they do not satisfy the criterion that their masses are above the mass limit given their redshifts. On the other hand, if the cluster masses are determined by the L_X–M scaling relation, the masses of the CC clusters will be biased high, and their inclusion in the mass function will lead to a shift toward higher values of Ω_M and σ_8.

F.A.S. acknowledges support from *Chandra* grant GO3-14131X. C.J., W.R.F., and A.V. are supported by the Smithsonian Institution. R.J.W. is supported by a Clay Fellowship awarded by the Harvard-Smithsonian Center for Astrophysics. Basic research in radio astronomy at the Naval Research Laboratory by S.G. and T.E.C. is supported by 6.1 base funding. S.B. acknowledges financial support from the PRIN-MIUR 201278X4FL grant. M.A., G.W.P., and J.D. acknowledge support from the European Research Council under the European Union's Seventh Framework Programme

Table 4
Concentration Parameter, Cuspiness, and Central Density for the *Planck* ESZ Sample

Cluster	R.A.	Decl.	z	C_{SB}	$\sigma_{C_{SB}}$	C_{SB4}	$\sigma_{C_{SB4}}$	δ	σ_δ	n_{core} (cm^{-3})	$\sigma_{n_{core}}$ (cm^{-3})	r_{max} (r_{500})
G000.44-41.83	21:04:18.603	−41:20:39.36	0.165	0.275	0.008	0.0585	0.0044	0.611	0.084	0.01482	0.00233	1.68
G002.74-56.18	22:18:39.822	−38:53:58.47	0.141	0.393	0.007	0.0604	0.0030	0.254	0.047	0.01423	0.00371	1.55
G003.90-59.41	22:34:27.334	−37:44:07.88	0.151	0.391	0.007	0.0335	0.0011	0.135	0.029	0.00729	0.00113	1.37
G006.47+50.54	15:10:56.117	+5:44:40.38	0.077	0.591	0.005	0.1674	0.0035	0.920	0.015	0.05946	0.00131	1.43
G006.70-35.54	20:34:46.912	−35:49:24.54	0.089	0.188	0.006	0.0334	0.0016	0.251	0.048	0.00469	0.00096	1.66
G006.78+30.46	16:15:46.073	−6:08:54.61	0.203	0.304	0.009	0.0250	0.0008	0.159	0.030	0.00819	0.00096	1.08
G008.30-64.75	22:58:48.095	−34:48:04.62	0.312	0.218	0.005	0.0422	0.0020	0.289	0.047	0.00831	0.00070	1.50
G008.44-56.35	22:17:45.701	−35:43:32.55	0.149	0.370	0.009	0.0939	0.0049	0.614	0.056	0.01607	0.00215	1.82
G008.93-81.23	0:14:19.305	−30:23:29.33	0.307	0.249	0.004	0.0273	0.0011	0.212	0.048	0.00813	0.00153	1.37

(This table is available in its entirety in machine-readable form.)

Table 5
Concentration Parameter, Cuspiness, and Central Density for the X-Ray Sample

Cluster	*Planck* Name	R.A.	Decl.	z	C_{SB}	$\sigma_{C_{SB}}$	C_{SB4}	$\sigma_{C_{SB4}}$	δ	σ_δ	n_{core} (cm^{-3})	$\sigma_{n_{core}}$ (cm^{-3})	r_{max} (r_{500})
2A0335	G176.28-35.05	03:38:40.698	+09:58:03.07	0.035	0.718	0.004	0.3876	0.0047	1.242	0.017	0.05916	0.00104	1.09
A85	G115.16-72.09	00:41:50.390	−09:18:09.53	0.056	0.455	0.004	0.1535	0.0030	1.012	0.040	0.04534	0.00113	1.40
A119	G125.58-64.14	00:56:16.210	−01:14:58.98	0.044	0.164	0.004	0.0229	0.0007	0.221	0.052	0.00258	0.00027	1.58
A133	G149.55-84.16[†]	01:02:41.707	−21:52:52.58	0.057	0.503	0.005	0.2421	0.0045	1.335	0.077	0.04650	0.00115	1.98
A193		01:25:07.559	+08:41:59.95	0.049	0.295	0.006	0.0596	0.0016	0.428	0.036	0.00825	0.00085	1.44
A376		02:46:03.910	+36:54:18.44	0.049	0.240	0.008	0.0870	0.0031	0.884	0.026	0.01538	0.00068	1.94
A399		02:57:53.422	+13:01:57.47	0.071	0.251	0.004	0.0357	0.0012	0.339	0.049	0.00643	0.00086	1.52
A401	G164.18-38.89	02:58:57.595	+13:34:44.19	0.074	0.308	0.005	0.0400	0.0012	0.262	0.040	0.00776	0.00081	1.34
A478	G182.44-28.29	04:13:25.196	+10:27:53.66	0.088	0.622	0.005	0.1726	0.0033	0.908	0.056	0.05973	0.00179	1.38
A496	G209.56-36.49	04:33:37.913	−13:15:42.03	0.033	0.438	0.005	0.1892	0.0039	1.200	0.086	0.04229	0.00359	0.79

(This table is available in its entirety in machine-readable form.)

(FP7/2007-2013)/ERC grant agreement n° 340519. L.L. acknowledges support from the *Chandra X-ray Observatory* grant GO3-14130B and by the *Chandra* X-ray Center through NASA contract NAS8-03060. We thank the anonymous referee for the useful comments.

Appendix

We present in Table 4 the values of the metrics for all clusters in the ESZ sample, including the secondary subclusters (on the lines following the primary subcluster, indicated by –). Columns list the cluster name (the prefix PLCKESZ is omitted for simplicity), R.A., decl., redshift, concentration parameter in the 0.15–1.0 r_{500} range, concentration parameter in the 40–400 kpc range, cuspiness of the gas density profile, central gas density, and the maximum radius where the emission integral is computed. Each metric value is followed by its uncertainty.

We present in Table 5 the values of the metrics for all clusters in the X-ray sample, including the secondary subclusters (on the lines following the primary subcluster, indicated by –). Columns list the cluster name, *Planck* name (the prefix PLCKESZ is omitted for simplicity; [†] the prefix PSZ1 is omitted for simplicity), R.A., decl., redshift, concentration parameter in the 0.15–1.0 r_{500} range, concentration parameter in the 40–400 kpc range, cuspiness of the gas density profile, central gas density, and the maximum radius where the emission integral is computed. Each metric value is followed by its uncertainty.

References

Allen, S. W., Evrard, A. E., & Mantz, A. B. 2011, ARA&A, 49, 409
Allen, S. W., & Fabian, A. C. 1998, MNRAS, 297, L57
Anders, E., & Grevesse, N. 1989, GeCoA, 53, 197
Andrade-Santos, F., Jones, C., Forman, W. R., et al. 2015, ApJ, 803, 108
Andrade-Santos, F., Jones, C., Forman, W. R., Lovisari, L. & Chandra-Planck Collaboration 2017, in American Astronomical Society Meeting Abstracts, #229, 404.04
Andrade-Santos, F., Lima Neto, G. B., & Laganá, T. F. 2012, ApJ, 746, 139
Andrade-Santos, F., Nulsen, P. E. J., Kraft, R. P., et al. 2013, ApJ, 766, 107
Andrade-Santos, F., Bogdán, Á, Romani, R. W., et al. 2016, ApJ, 826, 91
Angulo, R. E., Springel, V., White, S. D. M., et al. 2012, MNRAS, 426, 2046
Benson, B. A., de Haan, T., Dudley, J. P., et al. 2013, ApJ, 763, 147
Böhringer, H., Pratt, G. W., Arnaud, M., et al. 2010, A&A, 514, A32
Böhringer, H., Schuecker, P., Pratt, G. W., et al. 2007, A&A, 469, 363
Buote, D. A., & Tsai, J. C. 1996, ApJ, 458, 27
Cavagnolo, K. W., Donahue, M., Voit, G. M., & Sun, M. 2009, ApJS, 182, 12
Cavaliere, A., & Fusco-Femiano, R. 1976, A&A, 49, 137
David, L. P., Nulsen, P. E. J., McNamara, B. R., et al. 2001, ApJ, 557, 546
Ebeling, H., Edge, A. C., & Henry, J. P. 2001, ApJ, 553, 668
Eckert, D., Molendi, S., & Paltani, S. 2011, A&A, 526, A79
Fabian, A. C. 1994, ARA&A, 32, 277
Fabian, A. C. 2012, ARA&A, 50, 455
Fabian, A. C., & Nulsen, P. E. J. 1977, MNRAS, 180, 479
Fabian, A. C., Nulsen, P. E. J., & Canizares, C. R. 1984, Natur, 310, 733
Forman, W., & Jones, C. 1982, ARA&A, 20, 547
Hudson, D. S., Mittal, R., Reiprich, T. H., et al. 2010, A&A, 513, A37
Jeltema, T. E., Canizares, C. R., Bautz, M. W., & Buote, D. A. 2005, ApJ, 624, 606

Jones, C., & Forman, W. 1984, ApJ, 276, 38
Jones, C., & Forman, W. 1999, ApJ, 511, 65
Jones, C., Mandel, E., Schwarz, J., et al. 1979, ApJL, 234, L21
Jones, C., Santos, F. A., Forman, W. R., et al. 2016, in American Astronomical Society Meeting Abstracts, #228, 110.04
Kravtsov, A. V., & Borgani, S. 2012, ARA&A, 50, 353
Laganá, T. F., Andrade-Santos, F., & Lima Neto, G. B. 2010, A&A, 511, A15
Leccardi, A., Rossetti, M., & Molendi, S. 2010, A&A, 510, A82
Lin, H. W., McDonald, M., Benson, B., & Miller, E. 2015, ApJ, 802, 34
Mantz, A., Allen, S. W., Rapetti, D., & Ebeling, H. 2010, MNRAS, 406, 1759
Maughan, B. J., Giles, P. A., Randall, S. W., Jones, C., & Forman, W. R. 2012, MNRAS, 421, 1583
Mazzotta, P., Rasia, E., Moscardini, L., & Tormen, G. 2004, MNRAS, 354, 10
McDonald, M., Benson, B. A., Vikhlinin, A., et al. 2013, ApJ, 774, 23
Mohr, J. J., Evrard, A. E., Fabricant, D. G., & Geller, M. J. 1995, ApJ, 447, 8
Molendi, S., & Pizzolato, F. 2001, ApJ, 560, 194
Peterson, J. R., Kahn, S. M., Paerels, F. B. S., et al. 2003, ApJ, 590, 207
Piffaretti, R., Jetzer, P., & Schindler, S. 2003, A&A, 398, 41
Planck Collaboration, Ade, P. A. R., Aghanim, N., et al. 2011, A&A, 536, A8
Planck Collaboration, Ade, P. A. R., Aghanim, N., et al. 2013, A&A, 550, A130
Planck Collaboration, Ade, P. A. R., Aghanim, N., et al. 2014, A&A, 571, A20
Planck Collaboration, Ade, P. A. R., Aghanim, N., et al. 2016, A&A, 594, A24
Planck Collaboration, Aghanim, N., Arnaud, M., et al. 2011, A&A, 536, A9
Rasia, E., Borgani, S., Murante, G., et al. 2015, ApJL, 813, L17
Reiprich, T. H., & Böhringer, H. 2002, ApJ, 567, 716
Rossetti, M., Gastaldello, F., Eckert, D., et al. 2017, MNRAS, 468, 1917
Rossetti, M., Gastaldello, F., Ferioli, G., et al. 2016, MNRAS, 457, 4515
Santos, J. S., Rosati, P., Tozzi, P., et al. 2008, A&A, 483, 35
Sommer, M. W., & Basu, K. 2014, MNRAS, 437, 2163
Vikhlinin, A., Burenin, R., Forman, W. R., et al. 2007, in Heating versus Cooling in Galaxies and Clusters of Galaxies, ed. H. Böhringer et al. (Berlin: Springer), 48
Vikhlinin, A., Burenin, R. A., Ebeling, H., et al. 2009a, ApJ, 692, 1033
Vikhlinin, A., Kravtsov, A., Forman, W., et al. 2006, ApJ, 640, 691
Vikhlinin, A., Kravtsov, A. V., Burenin, R. A., et al. 2009b, ApJ, 692, 1060
Vikhlinin, A., Markevitch, M., Murray, S. S., et al. 2005, ApJ, 628, 655
Voevodkin, A., & Vikhlinin, A. 2004, ApJ, 601, 610
Warren, M. S., Abazajian, K., Holz, D. E., & Teodoro, L. 2006, ApJ, 646, 881
Wen, Z. L., & Han, J. L. 2013, MNRAS, 436, 275